
**1 Profiles of Wind Veer and Wind Speed in Turbulent
2 Ekman Flow**

3 Cedrick Ansorge, Hauke Wurps

4
5 Draft - Version June 27, 2024

6 Abstract

7 The profiles of wind speed and direction in turbulent Ekman flow are formulated
8 based on asymptotic theory and data from direct numerical simulation. The profile
9 of the streamwise component follows the classical viscous, logarithmic and wake
10 scaling. In the outer layer, the velocity component profiles can be described by an
11 Ekman-spiral with adapted boundary conditions that result in a reduction of the
12 spiral-like rotation. The span-wise component poses a conceptual challenge to the
13 channel-flow analogy in the context of asymptotic matching; it exhibits a mixed
14 scaling in the surface layer, but follows outer scaling for most of the outer layer.
15 Viscous stress scales universally across the boundary layer in inner units while
16 the total stress becomes universal as a function of outer height. This implies a
17 mixed scaling for the turbulent stress and eddy viscosity across the inner layer
18 and convergence to a universal scaling as function of the outer height across the
19 outer layer for increasing scale separation vide Reynolds numbers.

20 1 Introduction

21 The Coriolis force bends the path of motion on a rotating sphere and establishes
22 geostrophic equilibrium when in balance with a pressure gradient force. Wind veer
23 away from the wind direction in geostrophic equilibrium is (i) due to direct frictional
24 effects in the very vicinity of the surface and (ii) due to turbulence which
25 exerts indirect frictional effects; these effects cause a slow-down of the mean wind
26 reducing the Coriolis force thus turning the wind in favor of the pressure gradient
27 force. Not only does the veering set the frame of reference for surface layer theory,
28 it also has effects at small and large scales from large-scale dispersion via plume
29 spreading to cyclone spin-down (Svensson and Holtlag 2009) and on the capabilities
30 of data assimilation and accuracy of surface flux estimates (Brown et al.
31 2005). From a large-scale perspective, the veering of wind across the planetary
32 boundary layer determines the amount of cross-isobaric mass-flux, commonly referred
33 to as 'Ekman pumping' (Ekman 1905), and it is thus a key factor in the

Address(es) of author(s) should be given

34 life-cycle of large-scale synoptic systems. Within the atmospheric boundary layer
 35 (ABL), directional shear of the wind in the upper part of the surface layer may
 36 cause a systematic yaw for tall wind power generation devices where blades reach
 37 into the Ekman layer, i.e. that part of the boundary layer where the wind starts to
 38 turn; an exact estimate of such effects is critical in the site assessments for wind
 39 farms (Calaf et al. 2010; Mirocha et al. 2018).

40 In the planetary boundary layer, wind veer is characterized by the surface
 41 veering angle α defined as the angle between the negative surface shear stress
 42 τ_{sfc} and the geostrophic wind. Surface veering α and geostrophic drag $Z \equiv u_{\star}/G$,
 43 where the friction velocity $u_{\star} \equiv \sqrt{|\tau_{\text{sfc}}|/\rho}$, uniquely determine the surface drag τ_{sfc}
 44 in a turbulent Ekman flow. In any quantitative description of the surface layer, the
 45 friction velocity u_{\star} is the dynamic scale and α defines the alignment of the frame
 46 of reference. Knowledge about u_{\star} and α is thus a prerequisite for any quantitative
 47 theory of the surface layer, and Rossby and Montgomery (1935) constrained the
 48 two parameters based on integral relations in the ABL. Asymptotic similarity
 49 theory was later used by Tennekes (1973); Blackadar and Tennekes (1968), and—
 50 based on his seminal direct numerical simulations (DNS) of Ekman flow—, Spalart
 51 (1989) suggested a modification to take into account effects of low to intermediate
 52 Reynolds numbers. Later on, constants were re-evaluated with a focus on the ABL
 53 based on observations (Högström 1988, 1996) and numerical modelling (Spalart
 54 et al. 2008, 2009; Ansorge and Mellado 2014; Ansorge 2019).

55 Attempts were also undertaken to obtain profiles of the wind speed: One ap-
 56 proach is to match the inner and outer layer at a reference height; Etling (2002);
 57 Emeis (2018) (Sec. 21.10; Eq. 21.48) choose the Prandtl-layer height z_{Prandtl} to
 58 match the wind speed profiles, which, however, requires external prescription of
 59 $\alpha(z_{\text{prandtl}})$, the veering at that height. A one-dimensional profile with constant
 60 veering is given by Emeis et al. (2007, Sec. 3; Eq. 3.1-3.19).

61 Gryning et al. (2007) present an extension of the wind-speed profile beyond the
 62 surface layer using a neutral reference profile and a stability correction; Kelly and
 63 Gryning (2010), based on a probabilistic representation of stratification, develop
 64 a model for the long-term mean wind speed in the ABL and compare this with
 65 observation at different sites; Kelly and Troen (2016) demonstrate the effect of
 66 such improved model for wind-energy applications. In consideration of the large
 67 scale separation in geophysical flow, the rotation of the wind in the surface layer is
 68 often assumed negligible, and above investigations merely focus on the wind speed;
 69 that means, the veering of the wind with height is not described and there is little
 70 knowledge on the profile of the span-wise velocity component and the precise
 71 shape of the hodograph in the limit of a truly neutral Ekman boundary layer. A
 72 climatology of wind turning in the ABL is given by Lindvall and Svensson (2019)
 73 Klein et al. (2021) use a statistical turbulence modelling approach that yields a
 74 two-component velocity profile, but they also find that the exact representation of
 75 turning is challenging.

76 Ekman-layer models are roughly based on Ekman's seminal 1905 paper in
 77 combinations with additional assumptions, such as a prescribed profile shape for
 78 eddy viscosity Ellison (1955) and two-layer models of the ABL take into account
 79 rotational effects at higher altitudes, for instance when the wind speed needs to
 80 be evaluated at heights on the order of 100 – 200 m, a particular concern when
 81 it comes to wind-power forecasting (Optis et al. 2014). Despite rotational effects
 82 being considered, the formulation of these models for the outer layer and analysis

83 of their performance primarily focuses on wind speed. Still, in 2018, Jiang et al.
84 recognized that the outer part of the Ekman boundary layer receives less attention
85 in comparison with the surface layer and study the neutral problem by Large-Eddy
86 simulation (LES). They focus on the wind speed and find an extended logarithmic
87 layer when considering the wind speed instead of the shear-aligned component, and
88 they eventually demonstrate by means of an analytical model that this vertical
89 extension of the logarithmic layer may be explained by a transfer of stress to the
90 span-wise velocity component where it is assumed that the shear vector $\tau(z)$ and
91 stress vectors $(\partial_z U, \partial_z V)$ are aligned.

92 More recently, Ghannam and Bou-Zeid (2021) treated the horizontally av-
93 eraged momentum budget to show that departures from shear-alignment in the
94 vicinity of the surface result in an integral of the wind veer (α_M in their notation)
95 over the height to very high accuracy ($\int_{z_0}^H \sin \alpha_M$ in their notation; their Eq. (16)).
96 Classic surface-layer similarity is recovered when the angle α_M does not depend
97 on height, i.e., the wind veer is constant across the surface layer. If, however, the
98 wind veer depends on height, the profiles of stress and mean velocities depart from
99 the scalings implied by classic surface-layer similarity.

100 Turbulent Ekman flow is considered here as a conceptual model of the homo-
101 geneous, stationary ABL over a flat surface under neutral stratification. Universal
102 profiles of the wind vector for turbulent Ekman flow not only are a well-described
103 limit for theoretical exploration or higher-order approaches taking into account
104 possible effects of stratification, roughness or other physical complications encoun-
105 tered in the real geophysical system. While, on first sight, the study of such a
106 strongly idealized case appears as an academic problem, it contains the essence
107 of surface similarity as it is used in most atmospheric models, be it conceptual
108 or numeric ones. More complex accounts generally refer to the homogeneous sta-
109 tionary problem as a base state: (i) Roughness is commonly incorporated by a
110 linear transformation of vertical scale involving the roughness parameter z_0 and
111 for larger roughness also a displacement height (Monin and Yaglom 1975; Jacobs
112 and Van Boxel 1988; Högström 1988); (ii) Stability can be accounted for by a
113 linearization around the neutrally stratified profile (Monin 1970; Monin and Ya-
114 glom 1975; Högström 1988, 1996; Sakagami et al. 2020); (iii) Non-stationarity in
115 the pressure-gradient forcing can be accounted for by a linear damped-oscillator
116 approach around the base state (Momen and Bou-Zeid 2016); (iv) Barotropic and
117 baroclinic effects on the velocity profile require to consider the height-dependence
118 of the veer and stress misalignment (Momen et al. 2018; Ghannam and Bou-Zeid
119 2021). Furthermore, such a solution can serve as better initial condition for numer-
120 ical simulation of the flow, to minimize the length of initial transient periods, or
121 as benchmark for turbulence closures that can be tuned to reproduce the neutral
122 limit case.

123 Despite the strong simplifications implied by our choice of set-up, there is no
124 straightforward approach to solving this well-defined problem. Large-Eddy simula-
125 tion not only needs to be tuned for the surface shear stress and veering angle, but
126 it also relies on sub-grid closures that commonly assume alignment of the turbu-
127 lent stress with gradients. This pre-requisite is not fulfilled when the wind rotates
128 with height. Esau (2004) investigated the representation of the Ekman boundary
129 layer by dynamical subgrid closures and Zikanov et al. (2003) proposed a closure
130 for the wind profile using a linearized representation of the eddy viscosity. Despite
131 advances in analysis of this simplified set-up (Jiang et al. 2018), there is yet insuf-

132 ficient understanding for a quantitative generalization of the results to arbitrary
 133 external forcing (manifest in variation of the Reynolds number) – and indeed the
 134 fundamental questions pertaining to such relatively simple dynamics of turbulence
 135 are not reflected in the research on LES for the ABL over the past 50 years (Stoll
 136 et al. 2020).

137 At the same time, an increasing amount of high-quality and high-resolution
 138 data from turbulence-resolving approaches is emerging due to recent advances in
 139 high-performance computing and its application to geophysical problem sets; the
 140 geophysical range of scale separation, however, is—and it will remain so for the
 141 foreseeable future—out of reach for such simulation (Dimotakis 2005). Here, the
 142 routinely employed concept of Reynolds-number similarity can help. It postulates
 143 the existence of *fully developed turbulence* believed to occur for a sufficiently large
 144 but finite Reynolds number (Barenblatt and Goldenfeld 1995). (Already in 1998,
 145 this in fact lead Moin and Mahesh to the question *how high a Re is high enough?*)
 146 Certain statistics of fully developed turbulence, such as dissipation (Dimotakis
 147 2005) or profiles of mean velocity (Barenblatt 1993), become independent of the
 148 Reynolds number when appropriately scaled; other statistics, such as the near-
 149 wall maximum in velocity fluctuation depend on Re (Baars and Marusic 2020)
 150 and externality of the flow may exert an impact on near-wall scaling (da Silva
 151 et al. 2014). It appears that for certain statistics in Ekman flow, fully-developed
 152 turbulence is reached with the Reynolds numbers that became possible due to an
 153 increase of computing capabilities over the past decades.

154 This paper exploits the robust features of mean velocity profiles from direct
 155 numerical simulation across a range of Reynolds numbers to formulate both the
 156 streamwise and span-wise components of the mean velocity vector as a function
 157 of the Reynolds number.

158 2 Problem Formulation and Numerical Approach

159 We consider here incompressible, turbulent Ekman flow, that is, the turbulent flow
 160 over a flat rotating plate, as a physical model for the truly neutral ABL. The f-
 161 plane approximation is applied such that rotation only acts on horizontal velocity
 162 components; we thus neglect rotational effects on the horizontal components of
 163 velocity and dynamical effects due to latitudinal variation of the rate of rotation.

164 2.1 Notation and Governing Equations

165 The dimensional velocity vector of the numerical simulations is $\underline{U} = (U_1, U_2, U_3) =$
 166 (U, V, W) over the coordinate system $Oxyz$, where an approximate alignment
 167 (plus/ minus few degrees) of the direction Ox with the surface shear stress is
 168 achieved. The coordinate Oz points away from the wall, and Oy points in the
 169 span-wise direction normal to Oxz . For analysis of the results, we use two coordi-
 170 nate systems that are (i) exactly aligned with the surface shear stress

$$\tau_{\text{sfc}} = \begin{pmatrix} \tau_x \\ \tau_y \\ \tau_z \end{pmatrix} = -\nu \left(\frac{\partial U}{\partial z} \hat{e}_x + \frac{\partial V}{\partial z} \hat{e}_y \right) \quad (1a)$$

and labelled by an upper index α as in \underline{U}^α for the velocity vector, and (ii) the coordinate system aligned with the free-atmosphere geostrophic wind labelled by an upper index G as in \underline{U}^G . We denote the modulus of the surface shear, the surface friction, by

$$u_* = \sqrt{\|\underline{\tau}_{\text{sfc}}\|} \quad (1b)$$

and let $Z_* = G/u_*$; the surface veering angle α_* is the angle between $\underline{\tau}$ and the geostrophic wind

$$\alpha_* = \angle(\underline{G}, \underline{\tau}_{\text{sfc}}). \quad (1c)$$

Analogously, we denote the height-local veering of the wind $\alpha(z) = \angle(\underline{G}, \underline{U}(z))$, where $\underline{G} = (G_1, G_2, 0)$ is the geostrophic wind vector.

We consider the incompressible Navier–Stokes equations for the three velocity components on the f-plane in a framework that is governed by (i) geostrophic wind magnitude $G = \sqrt{G_1^2 + G_2^2}$, (ii) Coriolis parameter f (representing the angular rotation), and (iii) kinematic viscosity ν . In absence of external variability, this system converges to a statistically steady state in the sense that flow statistics do not depend on time; and this state is defined by a Reynolds number, the only non-dimensional parameter that governs the system. We use the geostrophic wind as velocity and the Coriolis parameter f as time scale for the non-dimensional framework. This implies the Rossby radius $A_{\text{Ro}} = G/f$ as length scale, such that one Reynolds number governing the problem reads as

$$\text{Re}_A = \frac{GA_{\text{Ro}}}{\nu}. \quad (2)$$

The scales used in defining Re_A are of limited relevance for description of the turbulent flow state. The turbulence scale separation in a wall-bounded flow is commonly characterized by the friction Reynolds number (?):

$$\text{Re}_\tau = \frac{u_* \delta}{\nu} = \delta^+ = \frac{\text{Re}_A}{Z_*^2}, \quad (3)$$

where $\delta = u_*/f$ and we use a superscript '+' to denote normalization by inner turbulence scales (u_*, ν) . Another common measure of scale separation is the Reynolds number defined by the laminar Ekman layer thickness $D = \sqrt{2\nu/f}$,

$$\text{Re}_D = \frac{GD}{\nu} = \sqrt{2\text{Re}_A}. \quad (4)$$

The governing equations non-dimensionalized by G , f , and A_{Ro} read as

$$\frac{\partial u_i}{\partial t} = \frac{\partial \pi}{\partial x_i} - u_j \frac{\partial u_i}{\partial x_j} + \epsilon_{ijl} (u_l - G_l) + \frac{1}{\text{Re}} \frac{\partial^2 u_i}{\partial x_j^2} \quad (5a)$$

$$\frac{\partial u_j}{\partial x_j} = 0, \quad (5b)$$

where $u_i = U_i/G$ are the non-dimensional components velocity, π is non-dimensional pressure, $g_j = G_j/G$ are non-dimensionalized components geostrophic wind (with $g_1^2 + g_2^2 = 1$ by construction), and ϵ is the Levi–Civita tensor. These equations are solved inside a bounded cube of size $L_x \times L_y \times L_z$ with periodic boundary conditions in the lateral (streamwise and spanwise) directions, a no-slip–no-penetration boundary at $z = 0$, and a no-penetration, free-slip boundary at $z = L_z$.

Table 1 Direct numerical simulation data sets used in this work. Re_A and Re_D refer to the Reynolds number defined in terms of the Rossby radius Λ and Ekman-layer thickness D respectively. L_{xy} is the domain size in the stream- and span-wise direction. The grid is given by the number of grid points in the stream-wise (N_x), span-wise (N_y) and vertical (N_z) directions respectively. The resolution in the span-wise and stream-wise directions are given as Δx^+ and Δy^+ . The grid in the vertical is stretched, and resolution at the wall is given by Δz^+ .

Re_A	Re_D	L_{xy}/Λ	$N_x \times N_y \times N_z$	Δx^+	Δy^+	$\Delta z^+ _{z=0}$
125 000	500	1.08	$2048 \times 2048 \times 192$	4.1	4.1	1.05
281 250	750	1.08	$3072 \times 3072 \times 384$	5.6	5.6	1.60
500 000	1 000	1.08	$3072 \times 6144 \times 512$	9.3	4.7	1.14
845 000	1 300	0.54	$2560 \times 5120 \times 640$	8.9	4.5	0.99
1 280 000	1 600	0.54	$3860 \times 7680 \times 960$	8.6	4.3	1.00

Table 2 DOIs and reference to the openly accessible data set at refubium repository

Re_D	DOI	Reference
500	10.17169/refubium-42505	Ansorge (2024a)
1000	10.17169/refubium-42507	Ansorge (2024b)
1300	10.17169/refubium-42508	Ansorge (2024c)
1600	10.17169/refubium-42509	Ansorge (2024d)

202 2.2 Numerical Simulations

203 The problem is solved numerically by tLab¹, an open-source tool-suite to simulate
 204 and analyze turbulent flows. We use here a fourth-order–five-step Runge–Kutta
 205 integration and sixth-order compact schemes for spatial derivatives in all direc-
 206 tions. The incompressibility constraint is enforced by a fractional step approach
 207 where the Poisson equation for the pressure field is solved to machine accuracy
 208 using a combined spectral/compact approach as described in Mellado and Ansorge
 209 (2012).

210 Simulations used here are shown in Tab. 1. We extend an existing set of simula-
 211 tions for $Re_A \in \{125\,000; 281\,250; 500\,000\}$ (gray shading; cf. Ansorge and Mellado
 212 2014, 2016) by new simulations at higher Reynolds numbers up to $Re_A = 1.28 \times 10^6$
 213 with a horizontal domain extent up to 3.3×10^4 viscous units. In total, this yields
 214 one order of magnitude variation in terms of the scale separation in the boundary
 215 layer.

216 3 Scaling behavior of the flow for Re_τ up to 3000

217 The generalization of profiles to arbitrary Reynolds numbers requires sufficient
 218 scale separation in the simulations, not only to quantify the effect of the Reynolds
 219 number on low-order flow statistics, but also to assess the corresponding rate-of-
 220 change to eventually allow for an extrapolation of the findings. While the simula-
 221 tions previously available (gray shading in Tab. 1) give confidence in a first-order
 222 representation of the turbulent problem, the estimation of higher-order effects
 223 such as the dependency of the Reynolds number requires a broader scale sepa-
 224 ration that is made available by the two new simulations at increased Reynolds
 225 number (cf. Tab. 1). Data at such scale separation has been obtained previously

¹ <https://github.com/turbulencia/tlab>

Table 3 Bulk characterization of the simulations for different Reynolds numbers Viscous Reynolds number Re , friction Reynolds number Re_τ , friction velocity u_* , surface veering angle α_* , normalized boundary layer depth δ_{95}/δ , inner normalization of vertically integrated TKE, outer normalization of vertically integrated dissipation.

Re	$\delta^+ = \text{Re}_\tau$	u_*	α_*	δ_{95}/δ	$f u_*^{-3} \int_0^\delta \epsilon dz$	$G^{-3} \int_0^\delta \epsilon dz$
500	479	0.0619	25.5	0.66	0.88	1.31
750	886	0.0561	21.0	0.65	0.90	1.34
1000	1403	0.0530	18.8	0.62	0.92	1.30
1300	2122	0.0501	17.9	0.59	0.85	1.24
1600	2978	0.0482	17.2	0.61	0.91	1.21

(cf. Spalart et al. 2008, 2009), but we also need high confidence with respect to the convergence of simulation data for slow oscillations and with respect to sampling convergence, which translates to two further requirements on the data: First, data should be free of artifacts from long-term oscillations across the vertical extent of the domain—primarily, simulations should be free of effects originating from the inertial oscillation; this is achieved here by replacing the mean value of the three-dimensional velocity fields by the time mean over a whole inertial oscillation. Second, high accuracy is also needed in terms of the statistical convergence of averages, bulk measures and large-scale structures; this requires a domain size $L_x > \mathcal{O}(\delta_{95})$. We use here $L_x = L_y = 1.08\Lambda$ for cases with $\text{Re} \leq 1000$ and $L_x = L_y = 0.54\Lambda$ for $\text{Re} \geq 1300$ which corresponds to $L_x/\delta_{95} \approx 25$ for $\text{Re}_D = 500$ and $L_x/\delta_{95} \approx 18$ for $\text{Re}_D = 1300$.

Bulk parameters of the simulations are given in Tab. 3. The surface stress is characterized by u_* and α_* in relation to the geostrophic wind vector and discussed in more detail as the drag law below in Sec. 4.1 (we find the expected slight decrease of u_* and α_* with increasing Re). The boundary-layer height estimated from the 95% stress reduction, δ_{95} , is around 0.6δ to 0.66δ . Interestingly, the integrated TKE $\int_0^\delta \epsilon dz$ stays constant when normalized by the friction velocity u_* while the integrated dissipation $\int_0^\delta \epsilon dz$ exhibits inviscid scaling when normalized by the magnitude G of the geostrophic wind. (TKE and dissipation normalized as $f G^{-3} \int \epsilon dz$ and $u_*^{-3} \int \epsilon dz$, exhibit substantial dependence on Re for the variation of u_* .) This indicates that the bulk dissipation is governed by the forcing G —irrespective of Re . Changes in Re , however, affect the level and organization of turbulence, and the parameter representing this dependency is the friction velocity u_* which describes the turbulence production processes in the surface layer, in particular in the buffer layer.

Velocity profiles in inner units ($U^+(z^+)$, Fig. 1a) and outer units ($U^-(z^-)$, Fig. 1b) are in accordance with previous work (Coleman et al. 1992; Spalart et al. 2008, 2009; Ansorge and Mellado 2014; Ansorge 2019): The profiles of the shear-aligned streamwise velocity component are well-collapsed for $\text{Re}_D > 500$ below $z^- \approx 0.15$ (circles in Fig. 1a); the case with $\text{Re}_D = 500$ is only transitionally turbulent and there is no distinct inner-outer scale separation. The logarithmic law is appropriate for $50 < z^+ < 0.15\text{Re}_\tau$, where $z^+ = \text{Re}_\tau z^-$. While the profiles $U^{\alpha_*+}(z^+)$ diverge between different Re beyond $z^- = 0.15$, the corresponding profiles of the velocity deficit ($U^{\alpha_*}(z^-) - G_1^\alpha$) agree closely, irrespective of Re . This illustrates the inner–outer scale-duality in this external flow with inner scaling

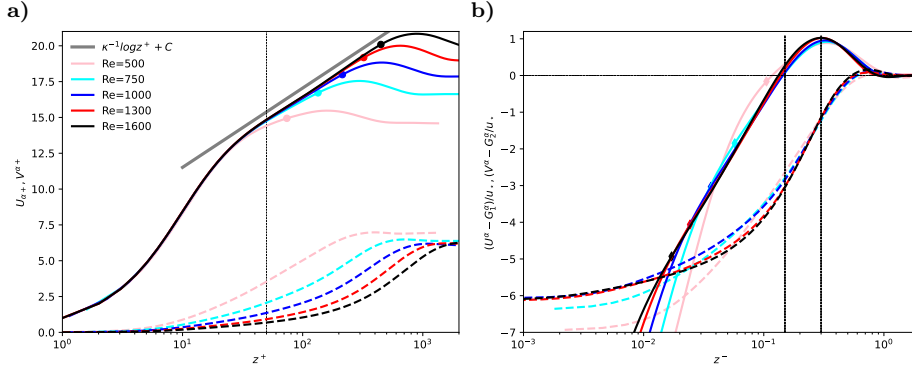


Fig. 1 a) Shear-aligned velocity profiles in inner units; b) Shear-aligned velocity deficit in outer units; circles mark the height $z^- = 0.15$; dashed line gives the best logarithmic fit to the data.

262 being appropriate in the inner layer and outer scaling in the outer layer. Also in
 263 the outer layer of the flow, u_* (and not the magnitude of the geostrophic wind
 264 G) governs the inviscid normalization, i.e. a scaling independent of the Reynolds-
 265 number.

266 No collapse in inner units is found for the profiles of spanwise velocity $V^{\alpha*+}(z^+)$.
 267 When normalized in outer units, the deficit profiles of spanwise velocity $(V^{\alpha*}(z^-) -$
 268 $G_2^\alpha)/u_*$ agree well beyond $z^- \approx 0.3$. This is a much higher level in comparison
 269 with the streamwise component that collapses also within the overlap layer, i.e.
 270 much closer to the surface (circles in Fig. 1b). The value of $V^{\alpha*+}(z^-) - G_2^\alpha$ is sen-
 271 sitive to the wind veering for $z \rightarrow 0$ as—for use of the shear-aligned component—it
 272 has to approach the value $-G_2^\alpha = |G| \sin \alpha \neq 0$ in view of the no-slip boundary
 273 condition. While low-Re effects appear to be present for $\mathcal{O}(\text{Re}) < 10^3$, the span-
 274 wise component converges to an Re-independent limit within the range of scale
 275 separation considered here, i.e.

$$G_2^\alpha/u_* = Z_* \sin \alpha \rightarrow \text{const. for } \text{Re} \rightarrow \infty, \quad (6)$$

276 which has indeed already been found by Spalart (1989), who estimates the constant
 277 from an integral relation.

278 The viscous stress

$$S_{\text{visc}} = \nu \sqrt{\left(\frac{\partial U}{\partial z} \right)^2 + \left(\frac{\partial V}{\partial z} \right)^2} \quad (7a)$$

279 exhibits universal scaling when considered as $S_{\text{visc}}^+(z^+)$ (Fig. 2a); this normaliza-
 280 tion is also appropriate in the outer layer where the viscous stress is, however,
 281 small. Small deviations from the universal profile are observed for the smallest
 282 Reynolds number $\text{Re} = 500$; we attribute these to low-Re effects in the only tran-
 283 sitionally turbulent flow ($\text{Re}_\tau = 479$). In contrast to the viscous stress, the total
 284 stress follows outer normalization, i.e. $S^+(z^-)$ is universal; a discrepancy in the
 285 inner layer does not occur as the total stress is approximately constant in the
 286 viscous and buffer layer, and a rescaling of the height would have no effect there;

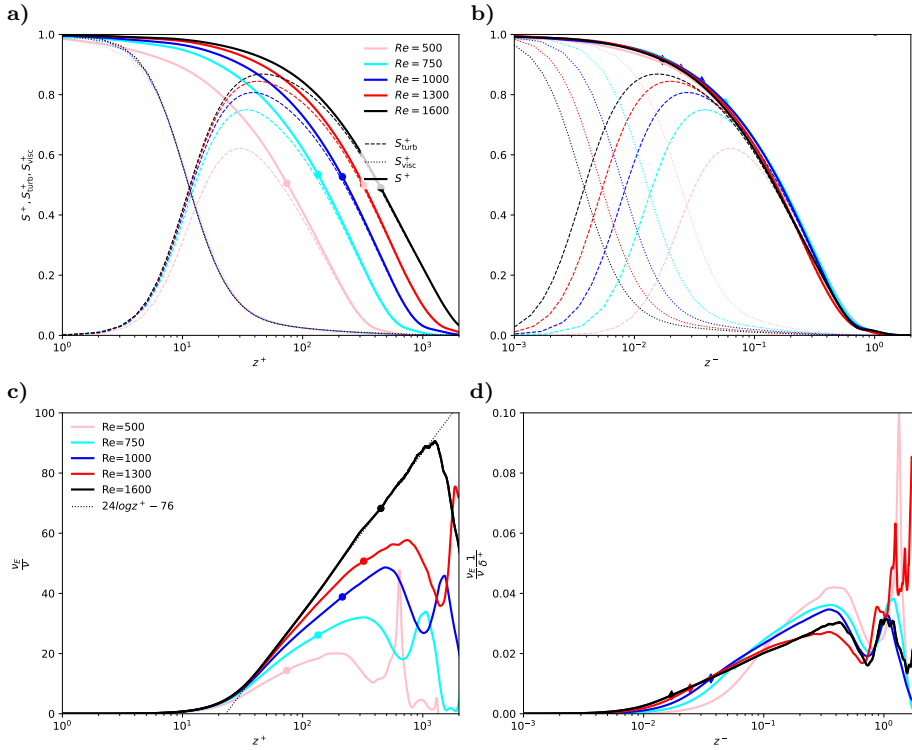


Fig. 2 a-b) Profiles of the turbulent stress S_{turb}^+ (dashed), the viscous stress S_{visc}^+ (dotted), and the total stress, $S^+ = S_{\text{visc}}^+ + S_{\text{turb}}^+$ (solid) as a function of inner height (a) and outer height (b). c-d) Normalized eddy viscosity ν_E (solid) plotted versus inner (c) and outer height (d). Different colors are for different Reynolds numbers (cf. Tab. 1). Circles in (a) and (c) denote the height $z^- = 0.15$, diamonds in (b) and (d) are for $z^+ = 50$ as in Fig. 1.

above, outer scaling is appropriate for the well-established dynamics in the overlap region of inner and outer layer. This, however, implies a mixed scaling for the turbulent stress,

$$S_{\text{turb}} = \sqrt{\overline{uw}^2 + \overline{vw}^2}. \quad (7b)$$

Indeed, S_{turb} only follows inner normalization below $z^+ \lesssim 20$ (where the turbulent contribution is negligible). In the outer layer, where $S_{\text{visc}} \rightarrow 0$, S_{turb}^+ follows outer normalization for $z^- \gtrsim 0.15$ —with increasing accuracy for larger Re and larger distance from the surface. In the overlap region, i.e. for $z^+ > 20$ and $z^- < 0.15$, the mixed scaling for the turbulent stress can be expressed as

$$S_{\text{turb}}^+(z^+, Re_\tau) = S^+(z^-) - S_{\text{visc}}^+(z^+), \quad (7c)$$

where $z^- = z^+/Re_\tau$.

The Eddy viscosity plays a crucial part when modelling profiles and the vertical transport in turbulent flow. In analogy to the Fick-law for molecular diffusion, the eddy diffusivity is the effective diffusivity that yields the turbulent transport S_{turb}

299 based on the strain rate. For the symmetries in the flow (horizontal homogeneity,
300 and $W = 0$), it is

$$\nu_E = \frac{S_{\text{turb}}}{\sqrt{\left(\frac{\partial U}{\partial z}\right)^2 + \left(\frac{\partial V}{\partial z}\right)^2}} = \nu \frac{S_{\text{turb}}}{S_{\text{visc}}}. \quad (8a)$$

301 The inner normalization of ν_E is obtained when dividing by the molecular viscosity:

$$\nu_E^+ = \nu_E / \nu = S_{\text{turb}} / S_{\text{visc}}. \quad (8b)$$

302 Under this normalization, the profiles of eddy viscosity collapse below $z^+ \approx 20$
303 with a tendency towards better collapse at higher z^+ for higher Reynolds number
304 (up to $z^+ \approx 50$ for $\text{Re} = 1600$; Fig. 2c). In the outer layer, the eddy viscosity
305 is characterized by a distinct minimum at $z^- \approx 0.6 - 0.8$, and we find that the
306 following mixed normalization of ν_E by the geostrophic wind and friction velocity
307 collapses the value of ν_E at this minimum (cf. Fig. 2d):

$$\nu_E^- = \nu_E^+ \frac{1}{\delta^+} = \nu_E \frac{1}{\nu} \frac{\nu}{u_* \delta} = \nu_E \frac{f}{u_*^2}. \quad (8c)$$

308 Substantial variation of the profiles is, however observed below and above this
309 minimum for different Re which illustrates that this normalization is probably not
310 generally appropriate across the outer layer.

311 The organization of the flow is depicted in terms of the turbulence kinetic en-
312 ergy in Fig. 3. In vicinity of the wall, at $y^+ \approx 10$, (Fig. 3a), elongated streaks
313 aligned with the surface shear stress dominate. Moving away from the wall, to
314 $y^+ \approx 150$ (well within the logarithmic region), the structures are larger and more
315 isotropic, but they are still largely aligned with the surface shear stress. In the
316 upper part of the outer layer, around $y^+ \approx 1000$, no clear signature of the sur-
317 face veering direction is found, and intense TKE structures (bright yellow) are
318 organized on a large spatial scale with weaker eddies (greenish structures) and
319 quiescent regions in between.

320 4 A universal velocity profile for the turbulent Ekman layer

321 We now turn to the formulation of a general velocity profile that is fully determined
322 by the only parameter of the idealized problem, namely a Reynolds number repre-
323 senting the scale separation or geometric size of the problem. This precludes, first,
324 a drag law wherewith we begin this section (4.1). Based on the scaling arguments
325 put forward in Sec. 3, we then develop, second, a formulation of the wind vector
326 in the Ekman layer (Sec 4.2). Finally, we come up with a separate formulation of
327 the, third, stream-wise and, fourth, span-wise velocity components in the overlap
328 and inner regions of the flow.

329 4.1 Drag-Law

330 A drag-law for Ekman flow determines—as a function of Reynolds number alone—
331 the surface drag. This can be formulated by the normalized surface friction, u_*
332 (Eq. (1b), also termed geostrophic drag), and the direction of surface shear stress,

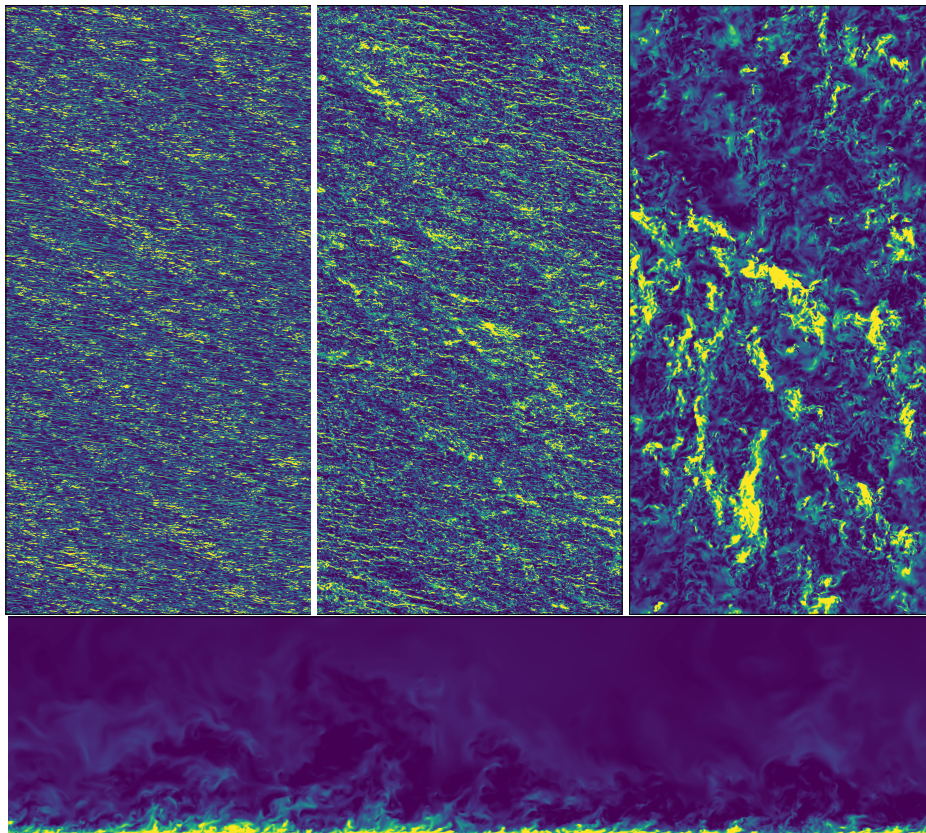


Fig. 3 horizontal slices of turbulence kinetic energy in the Buffer layer ($i=10$), logarithmic Layer ($i=100$), and outer layer ($i=400$); coloring between percentiles 4 and 96 of the respective image. Lower panel: streamwise–vertical intersect through the domain

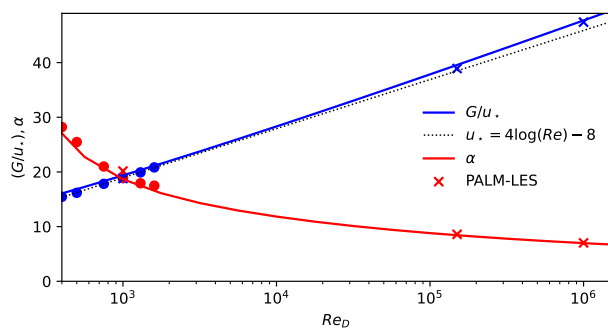


Fig. 4 Variation of geostrophic drag, Z_* , and surface veering, α_* , with Reynolds number according to the theory by Spalart et al. (1989) and as estimated from DNS data

³³³ α_* (Eq. (1c), also termed wind veer). A non-zero veering of the wind is a rather
³³⁴ special case in comparison with most turbulent flows considered in an engineering
³³⁵ context, and it confronts us with a situation where the most appropriate coordinate
³³⁶ system for analysis (namely that aligned with the surface shear stress) is a priori
³³⁷ unknown. We compare our DNS data against a semi-empirical drag-law based on
³³⁸ integral consideration (Spalart 1989) and find, as demonstrated in previous work
³³⁹ (Ansorge and Mellado 2014), excellent agreement in the range $400 < \text{Re} < 1600$,
³⁴⁰ representing a factor of 16 in variation of viscosity.

³⁴¹ We also find that the solution of the transient equation involved in estima-
³⁴² tion of u_* for a given Reynolds number Re_D is approximated reasonably by the
³⁴³ formulation

$$Z_* = 4 \log(\text{Re}_D) - 8 \quad (9)$$

³⁴⁴ which quantifies the 'weak' dependence of u_* on the Reynolds number as an ap-
³⁴⁵ proximately logarithmic one, at least for problems with a scale separation on the
³⁴⁶ order that is relevant to geophysical problems ($Re_D < 10^8$).

³⁴⁷ 4.2 Profile in the Ekman layer

³⁴⁸ Formulations for the outer layer that take into account the rotation (and thus
³⁴⁹ deviation from the channel-flow analogy) need to be matched to the framework of
³⁵⁰ surface similarity. A smooth transition from the inner layer to the Ekman layer,
³⁵¹ where the wind is characterized by a turning of its mean direction, is not easily
³⁵² achieved. Optis et al. (2014), for instance, define an "effective geostrophic wind
³⁵³ vector that has the same magnitude of the observed surface geostrophic wind and
³⁵⁴ is rotated by the angle α [their nomenclature]" to overcome the unsteady transi-
³⁵⁵ tion when approaching the Ekman layer from below. Such rotation of the wind
³⁵⁶ vector is *a posteriori* justified by the observational data that the model outcomes
³⁵⁷ are compared to. This need for a connection of the two reference frames is a man-
³⁵⁸ ifestation of a mismatch in the theoretical treatment of the inner and outer layer
³⁵⁹ in this rotating flow configuration.

³⁶⁰ The text-book solution for Ekman flow makes use of the physical boundary
³⁶¹ conditions (BCs) for the ABL (no-slip at the bottom and geostrophic wind in the
³⁶² free atmosphere) and a constant eddy viscosity. Specifying the boundary conditions
³⁶³ at top and bottom eliminates one mode of the analytical solution, and it determines
³⁶⁴ the magnitude of the spiral. In doing so, one has to assume that the solution
³⁶⁵ is appropriate across the entire ABL, which is not the case: The dynamics put
³⁶⁶ forth by Ekman in 1905 are not appropriate in the surface layer of the ABL;
³⁶⁷ better approximations exist for the logarithmic, buffer, and viscous sublayers. In
³⁶⁸ view of this situation, we use an adapted Ekman spiral that does not enforce the
³⁶⁹ boundary conditions at the surface but at a different height. This is achieved by
³⁷⁰ considering the Ekman spiral only in the Ekman layer, thus giving way for the
³⁷¹ well-established logarithmic and viscous-layer profiles in the lower surface layer.
³⁷² Based on the derivation in App. A, this profile is given by

$$\frac{1}{G} \begin{pmatrix} U_{ek} \\ V_{ek} \end{pmatrix} = \begin{pmatrix} 1 \\ 0 \end{pmatrix} + e^{-z_{ek}} \left[a_{ek} \begin{pmatrix} -\cos z_{ek} \\ \sin z_{ek} \end{pmatrix} + b_{ek} \begin{pmatrix} \sin z_{ek} \\ \cos z_{ek} \end{pmatrix} \right]. \quad (10a)$$

³⁷³ with $z_{ek} = \delta_{ek}(y^- - s_{ek})$. The right-hand-side consists of two modes with magni-
³⁷⁴ tude a_{ek} and b_{ek} shifted by $\pi/2$ with respect to each other. In the classic case, the

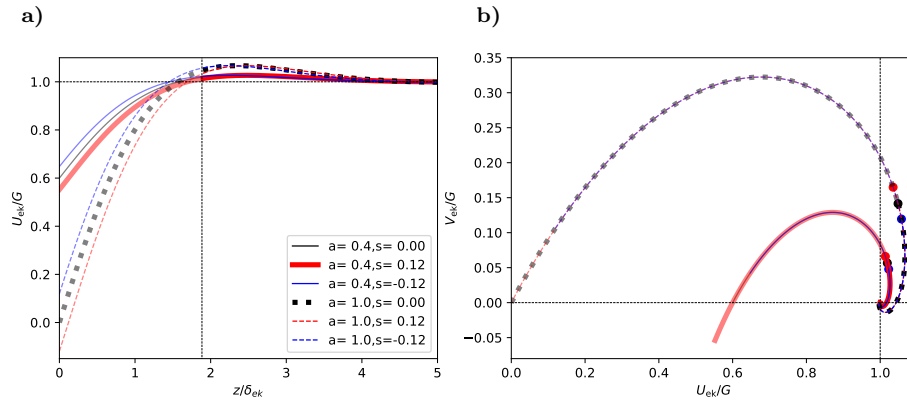


Fig. 5 a) Generalized Ekman-profile of the geostrophic-aligned component U_{ek} . b) Hodograph for the geostrophic-aligned and pressure-gradient aligned components U_{ek} and V_{ek} . Thick, black dashed line shows the classic solution. The height corresponding to $z^- = 0.30$ is marked by the dashed line in panel (a) and by filled circles in panel (b). The hodograph and profiles above this reference height are shown as solid lines, below as opaque line.

375 second mode governed by b_{ek} is incompatible with the surface boundary condition.
 376 While this is not the case here for the general form of the profile, the phase shifts
 377 can also be captured by the parameter s_{ek} , and we stick with to a single-modal
 378 approach, i.e., we let $b_{\text{ek}} = 0$.

379 This single-modal solution is characterized by three parameters, (i) an Ekman-
 380 layer depth scale δ_{ek} , (ii) the magnitude parameter of the spiral a_{ek} , and (iii) a
 381 zero-crossing point for the velocity s_{ek} . The effects of varying these parameters
 382 are illustrated in Fig. 5 where the classic Ekman solution is recovered by setting
 383 $a_{\text{ek}} = 1$, $s_{\text{ek}} = 0$ and $\delta_{\text{ek}} = \sqrt{2\nu/f}$. These parameters are *a priori* unknown as
 384 they need to conform to the turbulent state of the boundary layer; we use our
 385 DNS data to arrive at best estimates for them.

386 **The Ekman-layer depth scale** δ_{ek} is fundamentally defined by the eddy
 387 viscosity. However, we have seen in Section 3 that a characteristic value for the eddy
 388 diffusivity is not easily obtained for its strong dependence on the Reynolds number
 389 and distance from the surface. We therefore resort to the physical manifestation
 390 of the eddy diffusivity in an Ekman layer, and use the boundary layer depth
 391 $\delta_{\text{ek}} = 0.66\delta \times 2\pi$. For the relation $\delta_{\text{ek}} = \sqrt{2\nu_{\text{ek}}/f}$, this yields $\nu_{\text{ek}} \propto u_*^2/f$ in
 392 accordance with the observations in Sec. 3 (Eq. 8c).

393 **The magnitude parameter of the Ekman spiral**, a_{ek} , defines the super-
 394 geostrophic maximum of the wind profile aloft the logarithmic layer. Our sim-
 395 ulations suggest this maximum of the velocity deficit remains constant when nor-
 396 malized by u_* as shown in Fig. 6. The numerical value of a_{ek} is estimated from
 397 visual comparison, and we find $a_{\text{ek}} = 8.4u_*$; while this appears rather large, it
 398 is pre-multiplied by $e^{-z_{\text{ek}}}$ which has already decreased to $\mathcal{O}(0.1)$ at the height of
 399 this maximum. This choice ascertains that the velocity deficits $U/u_* - Z_*$ and
 400 $V/u_* - Z_*$ do not depend on the velocity scale u_* , but only on G as

$$U_{\text{ek}}/u_* - Z_* \propto a_{\text{ek}}Z_* = 8.4G. \quad (11)$$

401 Thus, the reduction of the area under the Ekman hodograph is directly linked to
 402 the variation in the friction velocity, which quantifies the well-known qualitative

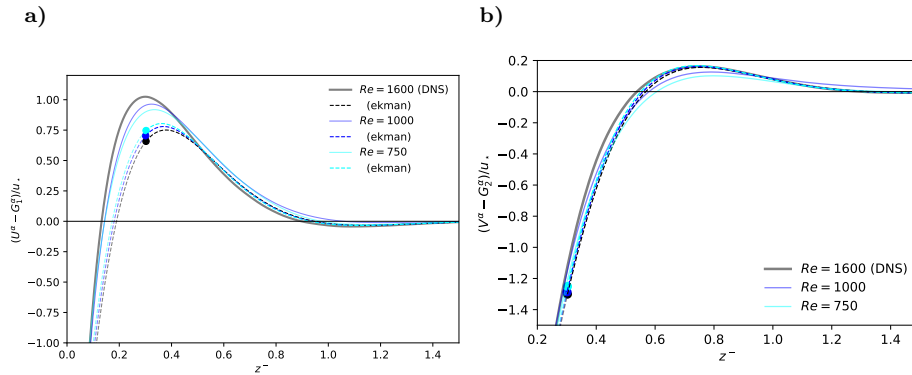


Fig. 6 Shear-aligned velocity deficit for the wall-streamwise (panel (a)) and wall-spanwise (panel (b)) components of the mean velocity U^{α} and V^{α} . Solid lines show DNS data, dashed lines the Ekman profiles U_{ek} and V_{ek} as defined in Eq. 10. Region below $z^- = 0.3$ is shown opaque. Variations in U_{ek} and V_{ek} are a consequence of the normalization and related to changes in u_* and α_* among the different Re_D .

403 observation that a more turbulent boundary layer leads to a flatter hodograph in
404 Ekman flow.

405 **The offset parameter** s_{ek} defines the zero-crossing height of the profile (in
406 contrast to δ_{ek} , which determines the thickness across which the wind veering
407 takes place). Physically, this offset can be understood as the height at which the
408 surface was located assuming a perfect Ekman flow down to the surface. As this
409 is not the case, and gradients are steeper in the highly turbulent boundary layer
410 flow encountered when approaching the surface, the offset is smaller than zero (the
411 fully turbulent boundary layer is actually thinner than an Ekman layer would be).
412 From our DNS data, we estimate $s_{\text{ek}} = -0.12$.

413 In summary, the outer layer of Ekman flow is characterized by a turning of
414 the wind velocity and the super-geostrophic maximum that is sustained by mo-
415 mentum convergence at the inflection point of the velocity profile. The super-
416 geostrophic maximum of streamwise velocity and a secondary minimum aloft the
417 bulk-turbulent part of the boundary layer are well-described by a classic Ekman
418 spiral with adapted boundary conditions and a shift in reference height. Corre-
419 sponding profiles are shown in comparison with data from three DNS runs in
420 Fig. 6. The idealized profiles capture the secondary minimum and convergence to
421 the geostrophic equilibrium in the non-turbulent flow very well.

422 4.3 Streamwise Velocity Component

423 For the streamwise velocity profile (that in non-rotating flows due to the geometry
424 is always aligned with the surface shear stress), well-established theories exist for
425 various regimes according to their distance from the wall and the relative role of
426 viscosity, turbulence and interaction with the outer region of the flow with the
427 logarithmic law for the mean velocity as a central anchor point.

428 In immediate vicinity to the surface, local turbulent mixing cannot occur for
429 the no-slip/no-penetration boundary condition, and the mean velocity is described

430 by a viscous profile of the form

$$U^{\alpha_*+} = z^+ \quad (12a)$$

431 where the direction of the velocity points into the exact opposite direction of the
 432 wall shear stress τ . In absence of roughness elements and for small roughness
 433 ($z_0^+ < 5$), this linear regime is known as viscous sub-layer Foken (2002); Foken
 434 et al. (1978). In fact, this law of the wall has no degree of freedom given the
 435 drag, i.e. once u_* and α_* are defined. However, theoretical foundation is lacking
 436 for the exact shape of the velocity profile in the buffer layer; though crucial for
 437 turbulence production, it is commonly understood as a transition region between
 438 the linear profile at the surface and the logarithmic profile aloft. A pure blending
 439 from the linear velocity profile into the logarithmic one is, however, not reasonable
 440 as both the linear and logarithmic profile overestimate the velocity in the buffer
 441 layer. We therefore introduce a two-step correction procedure, accounting for the
 442 smaller-than linear growth beyond $y^+ \approx 5$, and assuring smooth matching with
 443 the logarithmic law at $y^+ = 40$:

$$U_{\text{inner}}^{\alpha_*+} = \frac{z^+}{1 + c_1(y^+)^2} + (c_2y^+ - a_{\text{match}}) \frac{1 + \tanh[0.2(y^+ - 22)]}{2} + c_3 e^{-c_4(y^+ - 22)^2}. \quad (12b)$$

444 We use here

$$c_1 = 0.00185; \quad c_2 = 0.195; \quad c_3 = 0.4; \quad c_4 = 0.35.$$

445 The second and third terms on the right hand side vanish for $y^+ \ll 22$, and
 446 $c_1 = 0.00185$ implies an approximately 5% correction at $y^+ = 5$ and an 18.5%
 447 correction at $y^+ = 10$. The second and third term on the R.H.S. of eq. (12b) are
 448 an empirical fit to the velocity profiles observed in the buffer layer and appear
 449 independent of the Reynolds number for the range observed here. The coefficient
 450 a_{match} , which has no effect in the viscous sublayer, is then used to match this
 451 formulation to the logarithmic law employed above.

452 In the logarithmic region, we use the profile

$$U_{\log}^{\alpha_*+} = \frac{1}{\kappa} \log y^+ + C \quad (12c)$$

453 with the von-Kármán constant $\kappa = 0.416$ and the boundary condition $C = 5.4605$.
 454 For this logarithmic law, $a_{\text{match}} = 3.569861$ for a matching at $y^+ = 40$.

455 4.4 Spanwise velocity component

456 The background rotation and associated veering of the surface wind implies a
 457 non-zero profile for the span-wise velocity which challenges the conventional as-
 458 sumptions related to the channel-flow analogy: While the analogy with channel
 459 flow in vicinity of the wall implies that the streamwise component be zero or at
 460 least small, the veering requires a value of $V_{top} = U_G \sin \alpha_*$ in the free stream (and
 461 thus also at the top of the boundary layer if we assume that any substantial veloc-
 462 ity gradient is confined to the turbulent part of the flow). This continuous rotation
 463 of the wind vector is conveniently visualized by velocity hodographs aligned with

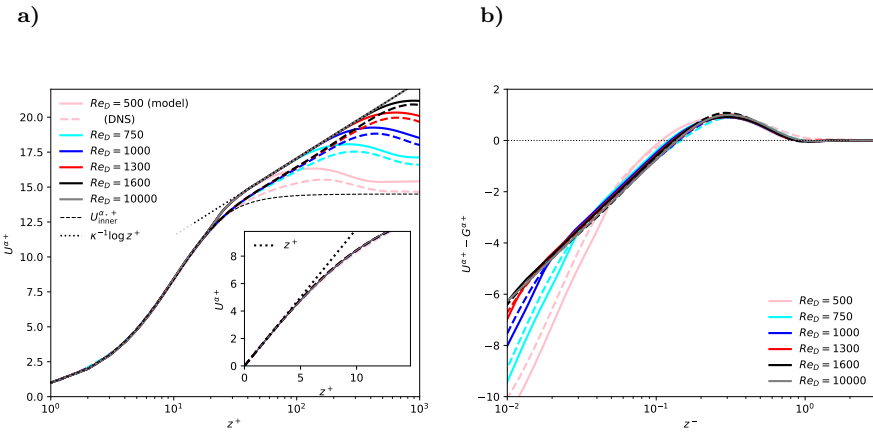


Fig. 7 Shear-aligned profiles of velocity components $U^{\alpha*+}$ in inner (left) and outer (right) units.

464 the outer, geostrophic flow (cf. Fig. 5b) and normalized by the geostrophic wind.
 465 The geometry of the flow and its drag imply the following for any hodograph: (i)
 466 the boundary conditions at the surface, (ii) the boundary condition at the top,
 467 and (iii) the inclination of the hodograph at the origin by the surface veering:

$$V^{\alpha*}(z=0)=0, \quad (13a)$$

$$\lim_{z \rightarrow \infty} V^{\alpha*} = G \sin \alpha_* \quad (13b)$$

$$\partial_{z^+} V^{\alpha*+} \Big|_{z=0} = 0. \quad (13c)$$

468 Outer scaling of the velocity profile further implies that the velocity deficit of
 469 $(V^{\alpha*} - G^{\alpha*})/u_*$ be a universal function of the outer height z^- . In the outer region
 470 of the flow (for $z^- \mapsto 1$), $f_V(z^-)$, should govern the spanwise velocity profile, as
 471 is supported by our DNS data (Fig. 1b); above $z^- \approx 0.3$, this profile is very well
 472 approximated by the Ekman-turning derived above (Eq. (10); Fig. 6b). While this
 473 deficit is a signature of outer rotation, it is inappropriate to extend this general
 474 relation to the surface where inner scales matter: On the one hand, the variation of
 475 the spanwise velocity deficit across the boundary layer (i.e. between $0 < z^- < 1$)
 476 must match the difference implied by the drag law (u_*, α_*) and the constant value
 477 of $V^{\alpha*}$ around $z^- = 0.3$. On the other hand, provided the outer velocity deficit
 478 is Re independent—the Re -dependence of α_* and u_* implies that this difference
 479 cannot be constant as a function of Re

480 We hence ask, how does the span-wise component scale when the surface is
 481 approached? Clearly, the spanwise contribution is small in comparison with the
 482 streamwise component throughout much of the layer below $z^- \approx 0.3$. However, we
 483 cannot assume $V = 0$ if a smooth matching between the inner and outer layers shall
 484 be achieved. In this context, we first realize that the velocity deficit $(V^{\alpha*} - G^{\alpha*})/u_*$
 485 approaches a Re -independent constant around $C_{V0} = Z_* \sin \alpha = 6.1$ at the surface;
 486 deviations from this constant are only found for the lowest Reynolds numbers
 487 which is in accordance with the low- Re correction suggested by Spalart (1989).
 488 This constrains the wind veer, and it quantitatively shows that the decreasing

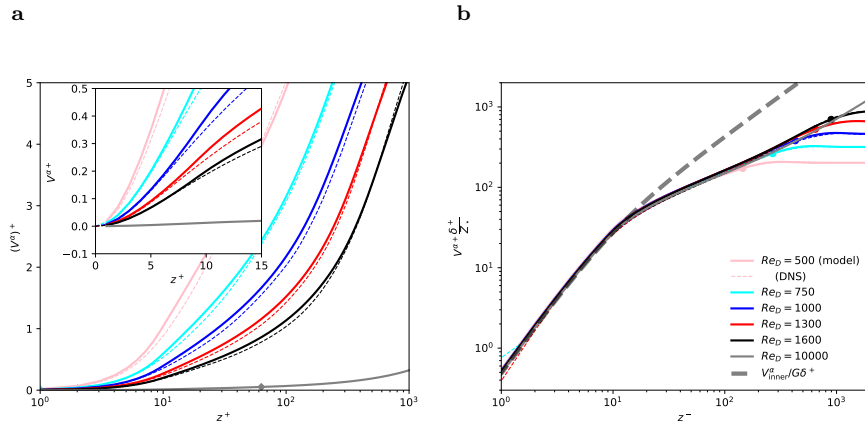


Fig. 8 Profiles of shear-aligned span-wise velocity $(W^\alpha)^+$ versus inner height. Dashed lines show DNS data, thick, opaque lines are from the semi-empirical theory developed above. Left panel shows standard inner normalization. Right panel shows the inviscid normalization yielding a universal profile for the spanwise component of velocity in the inner layer.

489 wall friction manifest in an increase of Z_* exactly compensates the decrease of
490 wind turning measured by $\sin \alpha_*$.

491 If the difference across the boundary layer is constant (C_{V0}) vs. Re , the av-
492 eraged gradient $\partial_{z^+} V^{\alpha*+}$ of the spanwise velocity component must decrease as
493 $1/\delta^+$ with increasing Re_τ . Hence, it should—at a fixed height—be $V^{\alpha*} \propto (\delta^+)^{-1}$.
494 A profile that agrees with the constraints of the profile at the surface and exploits
495 the dependence of $V^{\alpha*}$ on δ^+ is

$$V^{\alpha*} \frac{\delta^+}{G} = f_{V,\text{visc}}(z^+) = v_{\text{ref}} \left(\omega_v z^+ - 1 + \exp[-\omega_v z^+] \right), \quad (14)$$

496 where v_{ref} controls the magnitude of the profile and ω_v sets the height at which the
497 profile transitions into an approximately linear one. We find excellent agreement
498 with the DNS data for $500 \leq Re_D \leq 1600$ below $z^+ \approx 15$ with

$$v_{\text{ref}} = 18.85; \quad \omega_v = 0.2353$$

499 (cf. Fig. 8b).

500 For the adjacent surface layer, we find a log-like transition from the quasi-linear
501 profile inner profile around $z^+ = 10$ to a linear profile with increasing Re (Fig. 8b).
502 We model this transition by

$$f_{V,\log}(z^+) = \frac{V_{\log}(z^+)}{G} \delta^+ = a_{\log} + b_{\log} \log z^+ + c_{\log} z^+. \quad (15)$$

503 This surface-layer profile matches the inner (viscous) scaling in vicinity of the
504 surface to the outer (Ekman) scaling above $z^- = 0.3$ when constrained by the
505 viscous profile at the bottom and the Ekman profile at the top:

$$f_{V,\log}(z^+ = 10) = \quad f_{V,\text{visc}}(z^+ = 10) =: \quad v_{10} \simeq 27.3 \quad (16)$$

$$\frac{\partial}{\partial z^+} [f_{V,\log}]_{z^+ = 10} = \quad \frac{\partial}{\partial z^+} [f_{V,\text{visc}}]_{z^+ = 10} =: \quad d_{10} \simeq 4.01 \quad (17)$$

$$f_{V,\log}(z^+ = 0.3\delta^+) = \quad V_{\text{ek}}^{\alpha*}(z^- = 0.3)\delta^+ =: \quad v_{03} \quad (18)$$

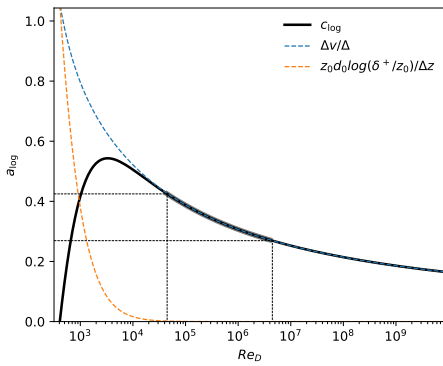


Fig. 9 c-log.

506 where v_{03} is determined by $V_{\text{ek}}(0.3)$ and $U_{\text{ek}}(0.3)$ and depends on Re . Given the
 507 Ekman formulation of the velocity profile introduced in Sec. 4.2, one may express
 508 v_{03} using the Ekman profile introduced in Sec. 4.2 together with the approximation
 509 for $u_*(\text{Re})$ found in Eq. (9). While the Re -dependency of a_{\log} , b_{\log} , c_{\log} is small,
 510 it shows up in Fig. 1 where the normalized profiles of spanwise velocity become
 511 more convex with increasing Re . We can now quantify this effect by means of the
 512 change of c_{\log} versus Re which is shown in Fig. 9 (cf. Appendix B; a_{\log} and b_{\log}
 513 are then determined by the universal values of v_{10} and d_{10}).

514 5 Discussion

515 5.1 Implications for surface-layer scaling

516 Eq. (14) establishes a universal mixed scaling for the spanwise velocity in the vis-
 517 ous layer: While it requires the vertical coordinate to be expressed in inner units,
 518 the velocity itself is normalized by the geostrophic wind, and becomes inversely
 519 proportional to the friction Reynolds number $\text{Re}_\tau = \delta^+$ when considered at a fixed
 520 height. In vicinity of the surface, such mixed scaling has already been identified
 521 for higher-order statistics in convective flows (Mellado et al. 2016; Li et al. 2018),
 522 where large scales leave their signatures in vicinity of the surface. It is important
 523 to note here that, while V is a first-order statistic from a statistical perspective,
 524 the spanwise velocity is a higher-order correction term from the perspective of sim-
 525 ilarity theory and from the viewpoint of the channel-flow analogy that is routinely
 526 employed in the surface layer. Further, this is consistent with the scaling for the
 527 velocity hodograph found in Eq. (11) where the friction velocity also drops out.

528 In the surface layer, there is not only a mixed scaling—as we had already iden-
 529 tified in the viscous layer—but we cannot find a universal function onto which the
 530 profiles of spanwise velocity collapse. This additional degree of freedom reflects the
 531 inner–outer matching problem for the spanwise velocity, and rather than giving a
 532 universal profile for this region, as is usually done, we resort here to a parametric
 533 description of the problem, namely in terms of the function $f_{V,\log}$ determined by
 534 the parameters a_{\log} , b_{\log} , c_{\log} which can be estimated based on the above scaling
 535 considerations for any Reynolds number. We note that, once the parameter a_{\log}

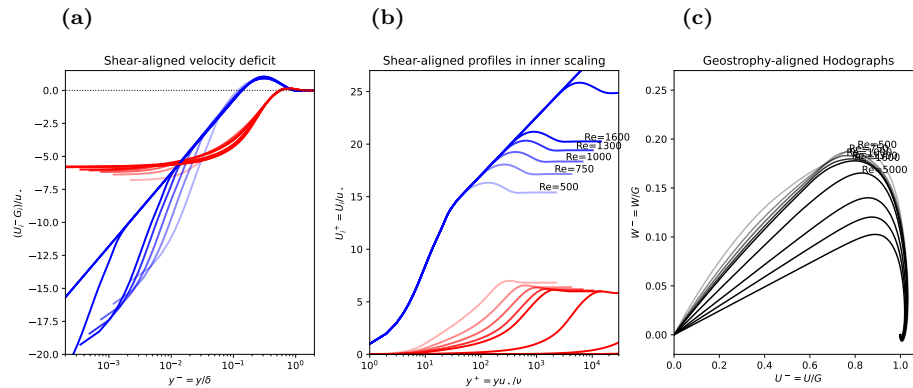


Fig. 10 (a) Velocity deficit, (b) velocity profile in shear-aligned hodographs and (c) hodograph in geostrophy-aligned coordinates. Thick, solid lines show theory, dashed lines data from DNS.

is known, the parameters b_{\log} and c_{\log} can be estimated solely based on $f_{V,\text{visc}}$, i.e. using the value v_{10} and d_{10} found for the viscous region of the flow. For the range of Reynolds number relevant to geophysical problems ($10^4 \lesssim \text{Re}_D \lesssim 10^6$), the variation of c_{\log} is, however, rather small.

540 5.2 Comparison with other theories

541 **Compare** to Emeis (2002) and Gryning (2007); highlight explicit knowledge on
542 veering-profile \rightarrow directional sheer;

543 **Compare** to van Driest scaling

544 **Remember** of interpretation in the context of eddy viscosity (Fig. 2) Consider
545 Townsend “Turbulent Shear Flow” Chapter 7.18: p. 319

546 Implications for **K-theory** (we now can consider that shear and stress are not
547 necessarily perfectly aligned). \rightarrow can we do something to infer a K-profile from
548 these theoretical considerations?

549 6 Conclusions

550 Applications:

- 551 – reference-shear for neutral profile approaches(systematic!) \rightarrow wind engineering!
- 552 – initial condition for LES/DNS to eliminate/minimize inertial oscillation in
553 Benchmark simulations

554 –

555 References

- 556 Ansorge C (2019) Scale Dependence of Atmosphere–Surface Coupling Through
557 Similarity Theory. Boundary-Layer Meteorol 170(1):1–27, DOI 10.1007/
558 s10546-018-0386-y

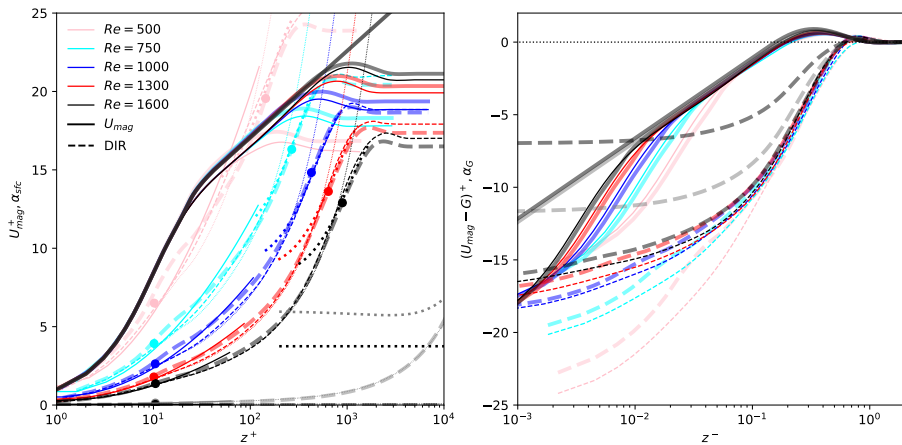


Fig. 11 Total velocity and veering (in degrees) vs inner and outer height. Dashed lines show DNS data, thick lines are from semi-empirical theory.

- Ansorge C (2024a) Direct numerical simulation of turbulent Ekman flow (Re=0500): DOI 10.17169/refubium-42505. DOI 10.17169/refubium-42505
 Ansorge C (2024b) Direct numerical simulation of turbulent Ekman flow (Re=1000): DOI 10.17169/refubium-42507. DOI 10.17169/refubium-42507
 Ansorge C (2024c) Direct numerical simulation of turbulent Ekman flow (Re=1300): DOI 10.17169/refubium-42508. DOI 10.17169/refubium-42508
 Ansorge C (2024d) Direct numerical simulation of turbulent Ekman flow (Re=1600); DOI 10.17169/refubium-42509. DOI 10.17169/refubium-42509
 Ansorge C, Mellado JP (2014) Global Intermittency and Collapsing Turbulence in the Stratified Planetary Boundary Layer. *Boundary-Layer Meteorol* 153(1):89–116, DOI 10.1007/s10546-014-9941-3
 Ansorge C, Mellado JP (2016) Analyses of external and global intermittency in the logarithmic layer of Ekman flow. *J Fluid Mech* 805:611–635, DOI 10.1017/jfm.2016.534
 Baars WJ, Marusic I (2020) Data-driven decomposition of the streamwise turbulence kinetic energy in boundary layers. Part 2. Integrated energy and. *J Fluid Mech* 882:A26, DOI 10.1017/jfm.2019.835
 Barenblatt GI (1993) Scaling laws for fully developed turbulent shear flows. Part 1. Basic hypotheses and analysis. *J Fluid Mech* 248:513–520, DOI 10.1017/S0022112093000874
 Barenblatt GI, Goldenfeld N (1995) Does fully developed turbulence exist? Reynolds number independence versus asymptotic covariance. *Phys Fluids* 7(12):3078–3082, DOI 10/bw2sq5
 Blackadar AK, Tennekes H (1968) Asymptotic Similarity in Neutral Barotropic Planetary Boundary Layers. *Journal of the Atmospheric Sciences* 25:1015–1020, DOI 10.1175/1520-0469(1968)025<1015:ASINBP>2.0.CO;2
 Brown AR, Beljaars ACM, Hersbach H, Hollingsworth A, Miller M, Vasiljevic D (2005) Wind turning across the marine atmospheric boundary layer. *Quarterly Journal of the Royal Meteorological Society* 131(607):1233–1250, DOI 10/dw2bxz

- 589 Calaf M, Meneveau C, Meyers J (2010) Large eddy simulation study of fully de-
590 veloped wind-turbine array boundary layers. *Phys Fluids* 22(1):015,110, DOI
591 10/b7gc6v
- 592 Coleman GN, Ferziger JH, Spalart PR (1992) Direct Simulation of the Stably
593 Stratified Turbulent Ekman Layer. *Journal of Fluid Mechanics* 244:677–712,
594 DOI 10.1017/S0022112092003264
- 595 da Silva CB, Hunt JC, Eames I, Westerweel J (2014) Interfacial Layers Between
596 Regions of Different Turbulence Intensity. *Annu Rev Fluid Mech* 46(1):567–590,
597 DOI 10.1146/annurev-fluid-010313-141357
- 598 Dimotakis PE (2005) TURBULENT MIXING. *Annual Review of Fluid Mechanics*
599 37(1):329–356, DOI 10.1146/annurev.fluid.36.050802.122015
- 600 Ekman VW (1905) On the influence of the earth's rotation on ocean currents. *Ark
601 Mat Astron Fys*, Vol 2 (1905), pp 1-53 2:1–53
- 602 Ellison TH (1955) The Ekman spiral. *Q J Roy Met Soc* 81(350):637–638, DOI
603 10.1002/qj.49708135025
- 604 Emeis S (2018) Wind Energy Meteorology, 2nd edn. *Atmospheric Physics for Wind
605 Power Generation*, Springer, Heidelberg
- 606 Emeis S, Baumann-Stanzer K, Piringer M, Kallistratova M, Kouznetsov R,
607 Yushkov V (2007) Wind and turbulence in the urban boundary layer analysis
608 from acoustic remote sensing data and fit to analytical relations. *metz* 16(4):393–
609 406, DOI 10.1127/0941-2948/2007/0217
- 610 Esau I (2004) Simulation of Ekman Boundary Layers by Large Eddy Model with
611 Dynamic Mixed Subfilter Closure. *Environmental Fluid Mechanics* 4(3):273–
612 303, DOI 10/b8f3kh
- 613 Etling D (2002) Theoretische Meteorologie, 2nd edn. *Eine Einführung*, Springer-
614 Verlag, Berlin, Heidelberg
- 615 Foken T (2002) Some aspects of the viscous sublayer. *metz* 11(4):267–272, DOI
616 10.1127/0941-2948/2002/0011-0267
- 617 Foken Th, Kitajgorodskij SA, Kuznecov OA (1978) On the dynamics of the
618 molecular temperature boundary layer above the sea. *Boundary-Layer Meteorol*
619 15(3):289–300, DOI 10.1007/BF02652602
- 620 Ghannam K, Bou-Zeid E (2021) Baroclinicity and directional shear explain depart-
621 ures from the logarithmic wind profile. *Quarterly Journal of the Royal Me-
622 teorological Society* 147:434–464, DOI 10/gnj6z2
- 623 Gryning SE, Batchvarova E, Brümmer B, Jørgensen H, Larsen S (2007) On
624 the extension of the wind profile over homogeneous terrain beyond the sur-
625 face boundary layer. *Boundary-Layer Meteorol* 124(2):251–268, DOI 10.1007/
626 s10546-007-9166-9
- 627 Högström U (1988) Non-dimensional wind and temperature profiles in the atmo-
628 spheric surface layer: A re-evaluation. *Boundary-Layer Meteorology* 42:55–78,
629 DOI 10.1007/BF00119875
- 630 Högström U (1996) Review of some basic characteristics of the atmospheric surface
631 layer. *Boundary-Layer Meteorology* 78(3-4):215–246, DOI 10.1007/BF00120937
- 632 Jacobs AF, Van Boxel JH (1988) Changes of the displacement height and rough-
633 ness length of maize during a growing season. *Agricultural Forest Meteorol*
634 42(1):53–62, DOI 10.1016/0168-1923(88)90066-4
- 635 Jiang Q, Wang S, Sullivan P (2018) Large-Eddy Simulation Study of Log Laws
636 in a Neutral Ekman Boundary Layer. *Journal of the Atmospheric Sciences*
637 75(6):1873–1889, DOI 10.1175/JAS-D-17-0153.1

- 638 Kelly M, Gryning SE (2010) Long-Term Mean Wind Profiles Based on
639 Similarity Theory. *Boundary-Layer Meteorol* 136(3):377–390, DOI 10.1007/
640 s10546-010-9509-9
- 641 Kelly M, Troen I (2016) Probabilistic stability and ‘tall’ wind profiles: Theory
642 and method for use in wind resource assessment. *Wind Energy* 19(2):227–241,
643 DOI 10.1002/we.1829
- 644 Klein M, Maier RE, Schmidt H (2021) Stochastic modeling of transient neutral
645 and stably-stratified Ekman boundary layers. *P A M M* 21(1):e202100,146, DOI
646 10.1002/pamm.202100146
- 647 Li Q, Gentine P, Mellado JP, McColl KA (2018) Implications of Nonlocal Trans-
648 port and Conditionally Averaged Statistics on Monin–Obukhov Similarity The-
649 ory and Townsend’s Attached Eddy Hypothesis. *J Atmos Sci* 75(10):3403–3431,
650 DOI 10.1175/JAS-D-17-0301.1
- 651 Lindvall J, Svensson G (2019) Wind turning in the atmospheric boundary layer
652 over land. *Q J Roy Met Soc* 145(724):3074–3088, DOI 10.1002/qj.3605
- 653 Marusic I, Monty JP, Hultmark M, Smits AJ (2013) On the logarithmic region in
654 wall turbulence. *J Fluid Mech* 716:R3, DOI 10.1017/jfm.2012.511
- 655 Mellado J, Ansorge C (2012) Factorization of the Fourier transform of the pressure-
656 Poisson equation using finite differences in colocated grids. *Z angew Math Mech*
657 92(5):380–392, DOI 10.1002/zamm.201100078
- 658 Mellado JP, van Heerwaarden CC, Garcia JR (2016) Near-Surface Effects of
659 Free Atmosphere Stratification in Free Convection. *Boundary-Layer Meteorol*
660 159(1):69–95, DOI 10.1007/s10546-015-0105-x
- 661 Mirocha JD, Churchfield MJ, Muñoz-Esparza D, Rai RK, Feng Y, Kosović B,
662 Haupt SE, Brown B, Ennis BL, Draxl C, Sanz Rodrigo J, Shaw WJ, Berg LK,
663 Moriarty PJ, Linn RR, Kotamarthi VR, Balakrishnan R, Cline JW, Robin-
664 son MC, Ananthan S (2018) Large-eddy simulation sensitivities to variations of
665 configuration and forcing parameters in canonical boundary-layer flows for wind
666 energy applications. *Wind Energy Science* 3(2):589–613, DOI 10/gn3nh4
- 667 Moin P, Mahesh K (1998) Direct numerical simulation: A tool in turbulence re-
668 search. *Annual Review of Fluid Mechanics* 30:539–578, DOI 10.1146/annurev.
669 fluid.30.1.539
- 670 Momen M, Bou-Zeid E (2016) Large-Eddy Simulations and Damped-Oscillator
671 Models of the Unsteady Ekman Boundary Layer*. *Journal of the Atmospheric
672 Sciences* 73(1):25–40, DOI 10.1175/JAS-D-15-0038.1
- 673 Momen M, Bou-Zeid E, Parlange MB, Giometto M (2018) Modulation of Mean
674 Wind and Turbulence in the Atmospheric Boundary Layer by Baroclinicity.
675 *Journal of the Atmospheric Sciences* 75(11):3797–3821, DOI 10/gfmn67
- 676 Monin AS (1970) The Atmospheric Boundary Layer. *Annual Review of Fluid
677 Mechanics* 2:225–250, DOI 10.1146/annurev.fl.02.010170.001301
- 678 Monin AS, Yaglom AM (1975) Statistical Fluid Mechanics, Vol. II, Dover Publi-
679 cations on Physics, vol II. Dover Publications, Inc., Mineola
- 680 Optis M, Monahan A, Bosveld FC (2014) Moving Beyond Monin-Obukhov Similar-
681 ity Theory in Modelling Wind-Speed Profiles in the Lower Atmospheric Bound-
682 ary Layer under Stable Stratification. *Boundary-Layer Meteorology* 153(3):497–
683 514, DOI 10.1007/s10546-014-9953-z
- 684 Rossby CG, Montgomery RB (1935) The layer of frictional influence in wind and
685 ocean currents. *Papers in Physical Oceanography and Meteorology* III(3):1–101

- 686 Sakagami Y, Haas R, Passos JC (2020) Generalized Non-dimensional Wind
 687 and Temperature Gradients in the Surface Layer. Boundary-Layer Meteorol
 688 175(3):441–451, DOI 10.1007/s10546-020-00510-3
- 689 Spalart PR (1989) Theoretical and numerical study of a three-dimensional turbu-
 690 lent boundary layer. J Fluid Mech 205(-1):319, DOI 10.1017/S0022112089002053
- 691 Spalart PR, Coleman GN, Johnstone R (2008) Direct numerical simulation of the
 692 Ekman layer: A step in Reynolds number, and cautious support for a log law
 693 with a shifted origin. Phys Fluids 20(10):101,507, DOI 10.1063/1.3005858
- 694 Spalart PR, Coleman GN, Johnstone R (2009) Retraction: “Direct numerical sim-
 695 ulation of the Ekman layer: A step in Reynolds number, and cautious support
 696 for a log law with a shifted origin” [Phys. Fluids 20, 101507 (2008)]. Phys Fluids
 697 21(10):109,901, DOI 10.1063/1.3247176
- 698 Stoll R, Gibbs JA, Salesky ST, Anderson W, Calaf M (2020) Large-Eddy Sim-
 699 ulation of the Atmospheric Boundary Layer. Boundary-Layer Meteorol 177(2-
 700 3):541–581, DOI 10/gmbmzw
- 701 Svensson G, Holtslag AAM (2009) Analysis of Model Results for the Turning
 702 of the Wind and Related Momentum Fluxes in the Stable Boundary Layer.
 703 Boundary-Layer Meteorol 132(2):261–277, DOI 10/bwknmt
- 704 Tennekes H (1973) A Model for the Dynamics of the Inversion Above a Convective
 705 Boundary Layer. Journal of the Atmospheric Sciences
- 706 Zikanov O, Slinn DN, Dhanak MR (2003) Large-eddy simulations of the wind-
 707 induced turbulent Ekman layer. J Fluid Mech 495:343–368, DOI 10/ccbpbw

708 **A Laminar Ekman solution with consideration of inner layer**

$$\begin{pmatrix} \partial_t U \\ \partial_t W \end{pmatrix} = \begin{pmatrix} fW & +\nu\partial_z^2 U \\ -f(U-G) & +\nu\partial_z^2 W \end{pmatrix} \quad (19a)$$

$$\Rightarrow \partial_t(U+iW) = f(W-i(U-G)) + \nu\partial_z^2(U+iW) \quad (19b)$$

709 In stationary conditions, this system is solved by

$$\hat{u}(z) = U_\infty + e^{-\gamma z} [A \cos \gamma z + B \sin \gamma z] \quad (19c)$$

$$\hat{w}(z) = W_\infty + e^{-\gamma z} [-A \sin \gamma z + B \cos \gamma z] \quad (19d)$$

710 where the constants U_∞ , W_∞ set the top boundary condition and A and B set the bottom
 711 boundary condition. The most common boundary condition for a surface Ekman layer is $A =$
 712 $U_\infty = G$, $B = 0$, and $W_\infty = 0$. The lower boundary condition, however, neglects the existence
 713 of the surface layer, and it appears reasonable to define $A = cG$ where $c < 1$ is a constant
 714 that incorporates the increased shear in the surface layer. Given a ‘matching height’ z_{match} and
 715 normalized matching height $\xi = \gamma z_{match}$ in the upper part of the inner layer, we can match
 716 the Ekman profile to the inner layer by letting

$$\begin{aligned} u(z_{match}) &\equiv u_{match} = U_\infty + e^{-\xi} [A \cos \xi + B \sin \xi] \\ w(z_{match}) &\equiv w_{match} = W_\infty + e^{-\xi} [-A \sin \xi + B \cos \xi] \end{aligned} \quad (20)$$

$$\Rightarrow \begin{pmatrix} u_{match} - U_\infty \\ w_{match} - W_\infty \end{pmatrix} = e^{-\xi} \begin{pmatrix} A \\ B \end{pmatrix} \begin{pmatrix} \cos \xi & +\sin \xi \\ -\sin \xi & +\cos \xi \end{pmatrix} \quad (21)$$

$$(22)$$

718 Matching the profile at $\xi = 0$, one obtains $A = \Delta u_{match}$ and $B = -\Delta w_{match}$; and when the
 719 direction Ox is aligned with the geostrophic wind, we obtain the textbook-case $A = |\mathbf{G}|$ and
 720 $B = 0$.

Otherwise, choosing $B \neq 0$ allows to introduce a phase shift of the Ekman rotation with respect to the decay of the wind spiral. As, however, in our context, the thickness and position of the spiral can already be controlled by the eddy viscosity and an offset in ζ , here we let $B = 0$.

725 B Matching the spanwise velocity profiles in the inner layer

726 The spanwise profile in vicinity of the surface is given by $V/G = f_{V,\text{visc}}\delta^+$ with

$$f_{V,\text{visc}} = v_{\text{ref}} (\omega_v z^+ - 1 + e^{-\omega_v z^+}) \quad (23a)$$

$$f_{V,\log} = a_{\log} + b_{\log} \log z^+ + c_{\log} z^+ \quad (23b)$$

727 Matching the profiles and gradient $z_0 = 10^+$ and the value at $z_1 = 0.3\delta^+$ yields

$$v_{\text{ref}} (\omega_v z_0 + e^{-\omega_v z_0}) = v_0 = a_{\log} + b_{\log} \log z_0 + c_{\log} z_0 \quad (24a)$$

$$v_1 = a_{\log} + b_{\log} \log z_1 + c_{\log} z_1 \quad (24b)$$

$$v_{\text{ref}} \omega_z (1 - e^{-\omega_z z_0}) = d_0 = \frac{b_{\log}}{z_{10}} + c_{\log} \quad (24c)$$

728 The gradient condition implies $b_{\log} = (d_0 - c_{\log})z_0$, and yields

$$v_0 - z_0 d_0 \log z_0 = a_{\log} + c_{\log} (z_0 - z_0 \log z_0) \quad (25a)$$

$$v_1 - z_0 d_0 \log z_1 = a_{\log} + c_{\log} (z_1 - z_0 \log z_0) \quad (25b)$$

$$\Rightarrow c_{\log} = \frac{\Delta v - z_0 d_0 \log z_1 / z_0}{\Delta z} \quad (25c)$$

729 with $\Delta z = z_1 - z_0$ and $\Delta v = v_1 - v_0$. Then, the coefficient a_{\log} is estimated as

$$a_{\log} = v_0 - z_0 d_0 \log z_0 - \frac{\Delta v - z_0 d_0 \log z_1 / z_0}{\Delta z} [z_0 - z_0 \log z_0]. \quad (25d)$$

730 We note that $\log(z_1/z_0)/(z_1 - z_0) \rightarrow 0$ for large z_1 , and as $z_1 = 0.3\delta^+$, this implies that the 731 second term in c_{\log} only plays a role at low and intermediate Re . Then, a_{\log} can be estimated 732 as

$$a_{\log} \simeq v_0 - z_0 \left[d_0 \log z_0 - \frac{\Delta v}{\Delta z} (1 - \log z_0) \right] \quad (25e)$$

733 for large Re .

734 A Old Stuff

735 **[OLD FROM HERE]** Below this region, the gradients in span-wise velocity are rather small and 736 the span-wise velocity monotonically approaches its surface boundary condition $V(z = 0) = 0$. 737 While the streamwise velocity follows a universal inner scaling that has acquired its universal, 738 Re -independent shape for $Re_D > \mathcal{O}(10^3)$, the span-wise component that defines how the 739 velocity vector veers when the surface is approached, does not collapse in inner units, and 740 there is, most importantly no sign of convergence even at the highest Reynolds numbers for 741 which simulations were carried out. Even though the simplest assumption $V = 0$ is reasonable 742 for the lower part of the surface surface layer ($z^- < 10^{-3}$), it does not appropriately capture 743 the profile in the rest of the surface layer:

744 First, $V = 0$ implies a discontinuity in the velocity profile at $z^- = 0.1$, where the outer 745 scaling found above yields a finite value at geophysical Re , i.e. there is non-zero veering in 746 the upper part of the surface layer—as is well-known also from field observation. Second, the 747 layer around $z^- = 0.1$ is crucial to obtain the characteristic and well-established shape of the 748 hodographs as the layer where V sets in marks the ‘maximum’ of V^- vs. U^- .

749 The scale for the magnitude of the span-wise velocity component is $u_* \sin \alpha$. Based on our
 750 DNS data, we suggest that the Reynolds number scaling of this velocity-magnitude scale is
 751 captured by $Re_\tau^{-1/2}$ which is indeed known from the generalization of higher-order statistics,
 752 such as turbulent fluxes in the inner layer (Marusic et al. 2013) that also follow a mixed scaling
 753 in the inner layer. We then parameterize the spanwise velocity at 10 wall units as anchor point
 754 in the inner layer:

$$V_{10} \equiv V(z^+ = 10) = 750 \frac{u_* \sin \alpha}{\sqrt{Re_\tau}}. \quad (26a)$$

755 This leaves us with three fixed points of the velocity profile in the inner layer, namely (i) the
 756 boundary condition $V_0 = 0$, (ii) V_{10} at $z^+ = 10$, and (iii) the lower end of the logarithmic
 757 profile at $z^- = 0.1$ where the latter two are semi-empirically estimated from DNS data. In
 758 absence of well-established scaling considerations for the span-wise velocity, the choice of profile
 759 fits joining these three points is indeed arbitrary, but we can resort to the DNS data for an
 760 empirical approach and find that a square-root profile fits $V(z^+)$ in the surface layer. A linear
 761 profile for V is employed in the viscous sub-layer. Based on the physical extent of the viscous
 762 sub-layer in Ekman flow around five wall units (Foken 2002; Ansorge 2019), we choose $z^+ = 5$
 763 to transition from one to the other and note that V is already very small at this height. The
 764 span-wise velocity profile in the surface layer is then estimated as

$$V(z^+) \Big|_{\text{inner}} = \begin{cases} a_1 z^+ & ; z^+ \leq 5 \\ b_1 + b_2 \sqrt{z^+} & ; 5 < z^+ < Re_\tau/10 \end{cases}, \quad (26b)$$

765 with b_1 and b_2 estimated such that

$$\begin{aligned} V(z^+ = 10) \Big|_{\text{inner}} &= V_{10} \\ V(z^+ = Re_\tau/10) \Big|_{\text{inner}} &= V_{\text{outer}}(0.1) \end{aligned} \Rightarrow \begin{cases} b_2 = \frac{V_{\text{outer}}(0.1) - V_{10}}{\sqrt{Re_\tau/10} - \sqrt{10}} \\ b_1 = V_{10} - \sqrt{10}b_2 \end{cases} \quad (26c)$$

766 We then estimate α from the matching condition at $z^+ = 5$, i.e.

$$5a = b_1 + \sqrt{5}b_2 \Rightarrow a = \frac{1}{5} \left[V_{10} + (\sqrt{5} - \sqrt{10}) \left(\frac{V_{\text{outer}} - V_{10}}{\sqrt{Re_\tau/10} - \sqrt{10}} \right) \right]. \quad (26d)$$

767 *Matching region.* While the profile composed of $V_{\text{inner}}(z^+ \leq 0.1Re_\tau)$, $V_{\text{outer}}(z^- > 0.1)$ is
 768 continuous, it is not smooth at $z^- = 0.1$, i.e. at the transition from power-law ($V \propto \sqrt{z^+}$)
 769 to logarithmic scaling. To alleviate this issue, we use a second-order polynomial for transition
 770 from the inner to the outer layer in the range $z_{\text{low}} < z < z_{\text{up}}$ such that

$$V_{\text{trans}}(z^-) = V_{\text{inner}}(z_{\text{low}}^+) + \Delta V (az_{\text{arg}} + b(z_{\text{arg}})^2) \quad (26e)$$

771 with $\Delta V = V_{\text{outer}}(z_{\text{up}}^-) - V_{\text{inner}}(z_{\text{low}}^+)$ and $z_{\text{arg}} = (z - z_{\text{low}})/(z_{\text{up}} - z_{\text{low}})$. It is $a + b = 1$ for
 772 $V_{\text{trans}}(z_{\text{up}}^-) = V_{\text{outer}}(z_{\text{up}}^-)$, and we constrain a by

$$\frac{\partial V_{\text{trans}}}{\partial z^-} \Big|_{z=z_{\text{low}}} = \frac{\partial V_{\text{inner}}}{\partial z^-} \Big|_{z=z_{\text{low}}}, \quad (26f)$$

773 where we find that $z_{\text{low}}^- = 0.06$ and $z_{\text{up}}^- = 0.13$ yield satisfactory agreement with DNS data.